Corrosion Science 76 (2013) 337–347

Contents lists available at SciVerse ScienceDirect

Corrosion Science

journal homepage: www.elsevier.com/locate/corsci

Erosion–corrosion of HVOF-sprayed Fe-based amorphous metallic coating under impingement by a sand-containing NaCl solution

Z.B. Zheng [a], Y.G. Zheng [a,*], W.H. Sun [b], J.Q. Wang [b]

[a] State Key Laboratory for Corrosion and Protection, Institute of Metal Research, Chinese Academy of Sciences, 62 Wencui Road, Shenyang 110016, PR China
[b] Shenyang National Laboratory for Materials Science, Institute of Metal Research, Chinese Academy of Sciences, 72 Wenhua Road, Shenyang 110016, PR China

ARTICLE INFO

Article history:
Received 14 May 2013
Accepted 2 July 2013
Available online 10 July 2013

Keywords:
A. Metal coatings
A. Stainless steel
B. Erosion
B. Polarisation
B. Potentiostatic
C. Passivity

ABSTRACT

Erosion–corrosion (E–C) behaviour of a Fe-based amorphous metallic coating (AMC) compared with 304 stainless steel (304 s.s.) was studied under a slurry impingement condition in a sand-containing NaCl solution. AMC exhibited much higher resistance to E–C than 304 s.s. The weight loss reached the maximum at an impact angle of 90° and the critical flow velocity was about 15 m/s for AMC, while 45° and 9 m/s for 304 s.s. The increment in passive current density under impingement for AMC was about 10 times lower than 304 s.s. Passive films formed at different impact velocities were of different thicknesses.

1. Introduction

Erosion–corrosion is a general cause of material deterioration of flow-handling components such as impeller, turbine, pump and pipe which work in solid particle-containing corrosive solutions at high flow rates. Two main effects are attributed to this behaviour: electrochemical corrosion and mechanical damage. Many researchers have shown that the synergies or interactions of the two effects play important roles in contributing to the total loss of materials. Based on this mechanism, new approaches to develop erosion–corrosion resistant materials may be discovered.

It is well known that bulk metallic glass has a disordered and low defects structure which makes it suitable for tribological and corrosive applications [1–3]. Unfortunately, size factor, poor plastic deformation after yielding and no work hardening during room temperature deformation significantly limit the possible application of it as a structural material [4]. Recently, high-velocity oxy-fuel (HVOF) Fe-based amorphous metallic coating (AMC) has attracted much attention [5,6]. Partial amorphous structure brings AMC superior corrosion resistance, both in Cl^- containing neutral solutions [7,8] and acidic solutions [9–11] due to a strong passivation capability. Meanwhile, AMC becomes more promising as a result of its high strength/hardness and excellent wear resistance [12]. As described above, erosion–corrosion is a complex combination of electrochemical corrosion and mechanical damage. The erosion–corrosion behaviour of the Fe-based amorphous metallic coating with good corrosion resistance and high hardness draws a lot of attention. But only a few researches focused on this area. Our earlier studies showed that Fe-based AMC exhibited better erosion–corrosion resistance than low carbon steel [13] and 304 s.s. [14] when working under sand-containing NaCl solutions using rotating disk equipment. More investigations should be further carried out to evaluate the erosion–corrosion resistance of Fe-based AMC.

Jet impingement methods have been commonly used by many researchers [15–19] to study the erosion–corrosion behaviour of materials under high-velocity sand containing solutions. They can provide accurate speeds of the impact streams and different impact angles. Two important parameters exist in an erosion–corrosion process: impact angle and flow velocity. Different materials may experience various degrees of damages at different impact angles. Some materials achieved the weight-loss peaks at oblique angles around 40° [20,21]. Other materials were damaged more severely at the normal angle [22]. Therefore, evaluating the erosion–corrosion behaviour of materials under different impact angles may narrow the gap between the experiments and the practical works. Flow velocity is another key parameter which affects the impact energy of particles and the erosion–corrosion behaviour of materials. It is believed that a critical flow velocity which results in the occurrence of depassivation on material surfaces exists in the erosion–corrosion progress [23–25]. This velocity is a critical parameter for the breakdown of passive film and a threshold where the transition from passive to erosion–corrosion regime

* Corresponding author. Tel.: +86 24 23928381; fax: +86 24 23894149.
E-mail address: ygzheng@imr.ac.cn (Y.G. Zheng).

0010-938X/$ - see front matter © 2013 Elsevier Ltd. All rights reserved.
http://dx.doi.org/10.1016/j.corsci.2013.07.006

starts for some materials. It can be used to evaluate the degrees of the erosion–corrosion resistance of different materials under slurry impingement.

In this work, a kind of Fe-based AMC sprayed on 304 s.s. by HVOF was prepared and the erosion–corrosion behaviour was investigated under slurry impingement by a sand-containing NaCl solution. To fulfill the mechanisms of impingement at different impact angles especially for the newly developed Fe-based AMC, effects of impact angles on weight losses of Fe-based AMC compared with 304 s.s. were studied. Electrochemical responses of the two materials were taken out to learn their depassivation behaviour under impingement. As the role of critical flow velocity under impingement remains ambiguous, a deep relationship between the critical flow velocity and the behaviour of passive film was studied in current work. Synergisms of corrosion and erosion for both Fe-based AMC and 304 s.s. were also stated here.

2. Experimental

2.1. Materials

The $Fe_{54.2}Cr_{18.3}Mo_{13.7}Mn_{2.0}W_{6.0}B_{3.3}C_{1.1}Si_{1.4}$ (wt.%) AMC based on 304 austenitic stainless steel in this work was prepared by high-velocity oxy-fuel thermal spray technology. The detail process was described in our previous work [26]. The base material was used for comparison. The test medium (to simulate the sand-containing seawater at Qinshan China [14]) was a slurry composed of 2 wt.% silica sand particles with the sizes of 75–150 mesh and 3.5 wt.% NaCl.

2.2. Characterisation of the coating

The microstructure of Fe-based AMC was detected by scanning electron microscopy (SEM) (FEI-Inspect F), energy dispersive spectroscopy (EDS), and transmission electron microscopy (TEM) (JME-2100F). X-ray diffraction (XRD) analyses of AMC were carried out by using an X-ray diffractometer (Rigaku D/max 2400) with copper Kα radiation. Percentages of the porosity and the oxide content were calculated using image analysis software on an optical microscopy (MEF-4). The thermal stability of AMC was examined by differential scanning calorimeter (DSC) (Perkin-Elmer DSC-7) in a continuous heating mode at a rate of 20 K min^{-1} under atmosphere. Micro-hardness was measured on the polished longitudinal sections of AMC and 304 s.s. using a micro-Vickers hardness tester (HVS-5). The hardness values were averages from five measurements around some similar areas to eliminate the artificial disturbance effects.

2.3. Erosion–corrosion test

The erosion–corrosion experiments were carried out using an impinging jet apparatus as shown in Fig. 1 and described in our previous work [22]. The velocity of the jet for the weight loss tests was kept constant at 20 m/s. In order to study the effect of the impact angles on erosion–corrosion, the angle was set at 30°, 45°, 60° and 90°, respectively. A liquid jet from a nozzle of 3 mm in diameter was impacted onto the centre of the test specimen. The stand-off distance between the jet nozzle exit and specimen surface was kept at 5 mm. The area of the specimen was 2.01 cm^2. The specimen surfaces of AMC and 304 s.s. were finally ground with 1000 grid abrasive papers then cleaned in alcohol and dried before the tests. After erosion–corrosion for 8 h, the specimens were degreased, rinsed, dried and finally weighted using an analytical balance with an accuracy of 0.1 mg. Each test was repeated at least three times to get reliable results.

2.4. Electrochemical measurements

Electrochemical measurements were conducted using a Potentiostat/Galvanostat (PARSTAT 2273). Before the tests, samples were ground with 240, 400, 600 and 1000 grid abrasive papers in sequence, degreased in alcohol, washed in distilled water and dried in air. During the tests, AMC or 304 s.s. was used as working electrode (WE), a saturated calomel electrode (SCE) was the reference electrode and a platinum plate was the counter electrode.

Static measurements were started after immersing the specimens in the 3.5 wt.% NaCl solution for about an hour to keep the open-circuit potentials stable. The in situ measurements under erosion–corrosion were conducted after erosion–corrosion for 10 min. Potentiodynamic polarisation was swept from −1000 to +1500 mV versus the open-circuit potential at a rate of 0.5 mV s^{-1}. In order to investigate the depassivation of the materials under erosion–corrosion, an appropriate potential in the passive region of the two materials according to the results of the polarisation was used to perform the potentiostatic measurements. The velocities applied in these measurements varied as shown in Fig. 2. At least two replicate tests were carried out to determine the experimental errors.

2.5. Surface analyses

The morphological observations of the specimens' surfaces after erosion–corrosion tests at different angles were done by using a Confocal Laser Scanning Microscope (CLSM) (LEXT-OLS4000). The overall damages could be detected visually through this method. The quantitative information on the damage depth was also carried out by measuring a parameter R_{max} which was defined as the largest distance between the peak and valley of a measuring length using the CLSM. The micro-morphologies of the damages were observed by SEM. To understand the repassivation behaviour of the materials under erosion–corrosion, X-ray photoelectron spectroscopy (XPS) was employed by using ESCALAB 250 photoelectron spectrometer with Al Kα excitation ($h\gamma$ = 1486.6 eV). Binding energies were calibrated using carbon contamination with C1s peak value of 284.6 eV. XPS ion beam sputtering with argon was used to analyse the depth profiles of AMC's surfaces and the sputter rate was 0.1 nm s^{-1}.

3. Results

3.1. Characterisation of the coating

Fig. 3a shows the typical regions from cross-sections of Fe-based AMC. The coating with a thickness of about 500 μm adheres well to the substrate and presents a dense structure. In the picture of high magnification (Fig. 3b), un-melted particles, oxides and pores can be found out. It is notable that the oxides are enrichment in the linear phases from the results of EDS, which is similar to Guo's work [27]. Three credible regions were tested to calculate the percentages of the porosity and the oxide content and the mean values are 1.5% and 2.0% respectively, which are typical values for coatings fabricated by HVOF.

The XRD pattern of the coating is shown in Fig. 3c, followed by the DSC result in Fig. 3d. A broad peak appears in the XRD pattern and it stands for an amorphous structure of the coating. Besides, crystalline phases are detected out with a major composition of Fe_2C. The amorphous structure indicates that this Fe-based coating has a great glass formation ability (GFA) which may be related to the supercooled liquid region (SLR). The supercooling is defined as the difference between the glass transition temperature (T_g, about 640 °C in current work) and the onset temperature of

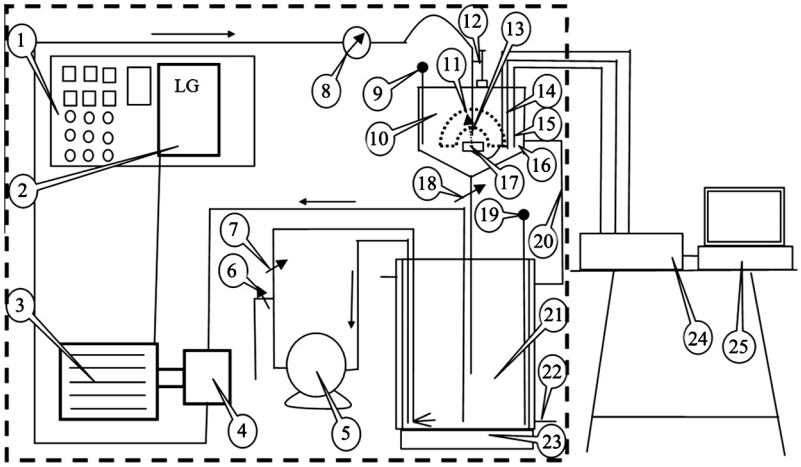

Fig. 1. Schematic diagram of the jet impingement apparatus for erosion–corrosion. (1) Control cabinet; (2) frequency converter; (3) motor; (4) lobular pump; (5) stirring pump; (6 and 7) valves; (8) screw elevator; (9) thermocouple I; (10) impingement cabinet; (11) impingement angle meter; (12) electromagnetic flowmeter; (13) nuzzle; (14) reference electrode; (15) counter electrode; (16) pH meter probe; (17) sample (working electrode); (18) valve; (19) thermocouple II; (20) overflow tube; (21) slurry container; (22) cooling water; (23) heater; (24) electrochemical workstation and (25) computer.

crystallisation (T_x, about 690 °C in current work). According to the result of DSC in present work, the supercooling of Fe-based AMC is about 50 °C, which indicates a high thermodynamic stability [28,29].

More detail information on the structure of the AMC was obtained by TEM. Two different regions in coating were taken out as shown in Fig. 4. The diffused halo rings in the selected area diffraction pattern of Fig. 4a states that AMC is basically composed of amorphous phase which is consistent with the result from XRD. Crystalline phases are detected out as depicted in Fig. 4a and nanocrystalline grains are also found out in Fig. 4b by the specific diffraction pattern. The generation of the crystalline phases and nanocrystalline grains may be caused by the heats accumulated inside the coating [7].

Fig. 5 is the micro-hardness distribution along the depth of a cross-section of the substrate stainless steel and AMC. The hardness of AMC is more than four times that of 304 s.s. This may be the reason why AMC has higher wear resistance and erosion–corrosion resistance than stainless steel [30].

3.2. Potentiodynamic tests

Fig. 6 shows the potentiodynamic curves measured under a static condition (Fig. 6a) and a slurry impingement (Fig. 6b) at 20 m/s in a NaCl solution of both AMC and 304 s.s. The impact angle was kept at 90°. Table 1 gives some corrosion properties extracted from the potentiodynamic curves. The corrosion potential (E_{corr}) and corrosion current density (i_{corr}) were carried out using a suitable fitting procedure by Cview software. The current density at the passive stage (i_p) was derived by averaging current densities in the passive region [31]. Data in Table 1 shows that the corrosion current density of stainless steel (0.16 μA/cm^2) is lower than that of AMC (1.25 μA/cm^2) in the static 3.5 wt.% NaCl solution. The contrast indicates that 304 s.s. has a better uniform corrosion resistance than AMC. While taking the pitting potential (E_b) into consideration, AMC (1.012 V) is much higher than 304 s.s. (0.365 V), which demonstrates that AMC shows relatively higher pitting corrosion resistance than 304 s.s., similar results are seen in other researches [26,32]. It is interesting to analyse the potentiodynamic curves under slurry impingement as shown in Fig. 6b. In general, the curves shift toward a higher current density and a lower potential compare to the curves under static condition. The acceleration of corrosion is resulted from erosion. It is notable that the corrosion acceleration for 304 s.s. under impingement is more serious from the changes of the i_{corr} and i_p which increase about 100 times while only 10 times for AMC. Under the impingement of a slurry of 2 wt.% silica sand and 3.5 wt.% NaCl at 20 m/s, the passive current density of AMC is a little lower than that of 304 s.s., which is different from the result under static condition (Fig. 6a). Another parameter E_b, as shown in Table 1, displays different changes for AMC and 304 s.s. The reduction of E_b for 304 s.s. stands for an easier pitting corrosion under impingement than static condition. While the value of AMC keeps almost the same from static condition to impingement condition. Sasaki and Burstein [17] studied the erosion–corrosion of stainless steel under impingement by a fluid jet and found that impact by a fluid jet played two apparently opposing roles in pitting corrosion. On one side, fluid jet impingement impeded evolution of stable pits. On the other side, fluid jet impingement accelerated pitting corrosion. In present work, with a high flow velocity (20 m/s) and sand-containing solution, the latter effect dominates as concluding from the potentiodynamic tests. From the view of the protective passive film, it comes to an inference that the passive film formed on AMC has a better protectiveness than the passive film formed on 304 s.s. under high speed impingement by a sand-containing NaCl solution.

3.3. Erosion–corrosion at different impact angles

Fig. 7 shows the comparison of the cumulative weight losses of 304 s.s. and AMC at different impact angles after slurry impingement

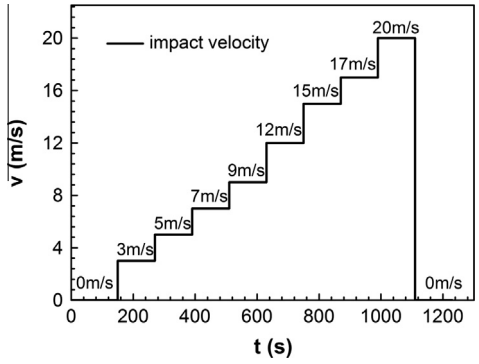

Fig. 2. Impact velocity of samples corresponding to time curves.

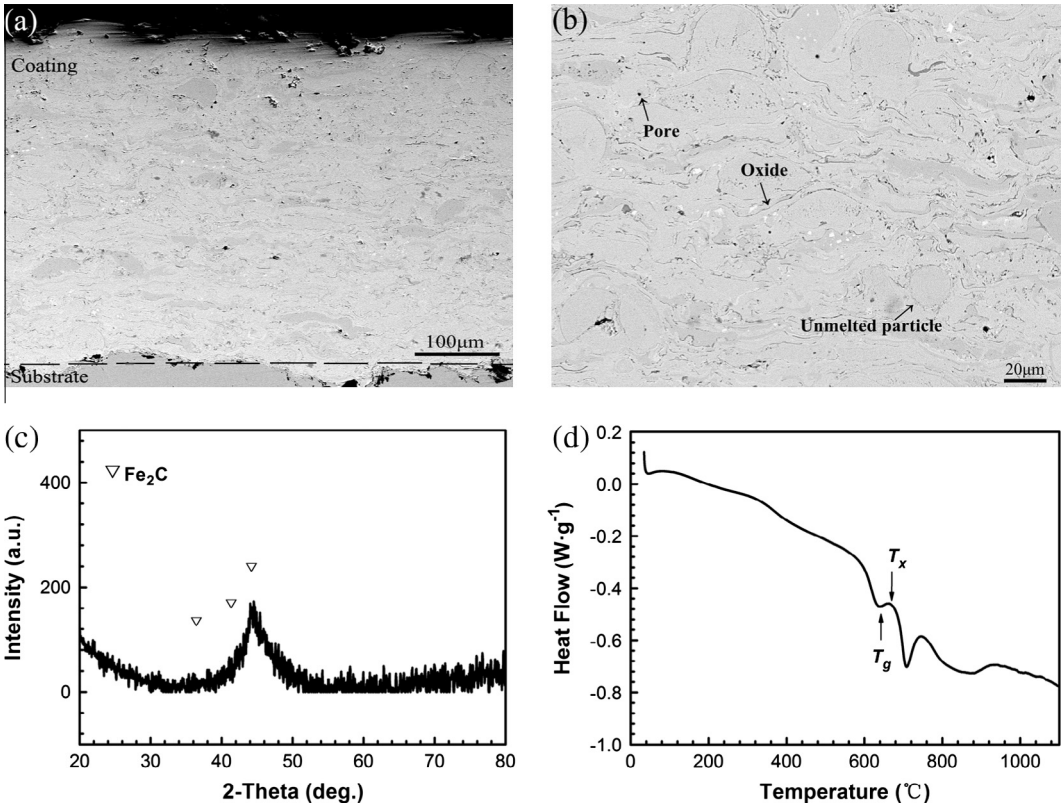

Fig. 3. (a and b) SEM micrograph from cross-section of the as-deposited Fe-based AMC; (c) XRD pattern of Fe-based AMC and (d) DSC curve of Fe-based AMC.

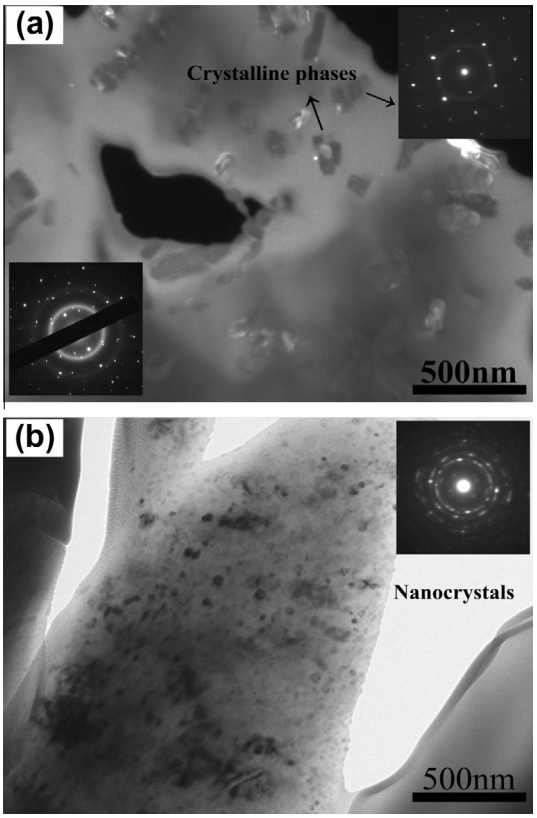

Fig. 4. Bright-field TEM images and selected area electron diffraction (SAED) patterns of the coating.

for 8 h. It is apparently that the maximum erosion–corrosion rate of 304 s.s. occurs at the impact angle of around 45°, which is consistent with the work by Tang et al. [21] who observed that the weight loss peak appeared at the impact angle of 45° for X-65 steel in the simulated oil-sand slurry and other works [33,34]. In contrast to 304 s.s., Fe-based AMC presents better erosion–corrosion resistance from the results of the weight losses. The weight loss of 304 s.s. (2.6 mg) is more than 8 times that of AMC (0.3 mg) at the impact angle of 45° especially. The severest damage of AMC approximates the slightest damage of 304 s.s. under impingement at different impact angles. The result also displays a trend that the cumulative weight loss of AMC shows an increase with the impact angle and reaches the maximum at 90°, which may attribute to the high hardness and the brittleness of AMC [35,36].

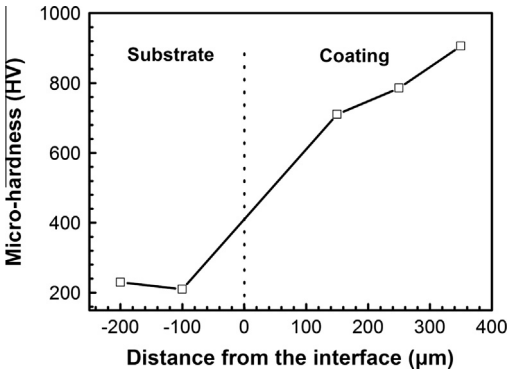

Fig. 5. Micro-hardness of AMC and the substrate stainless steel.

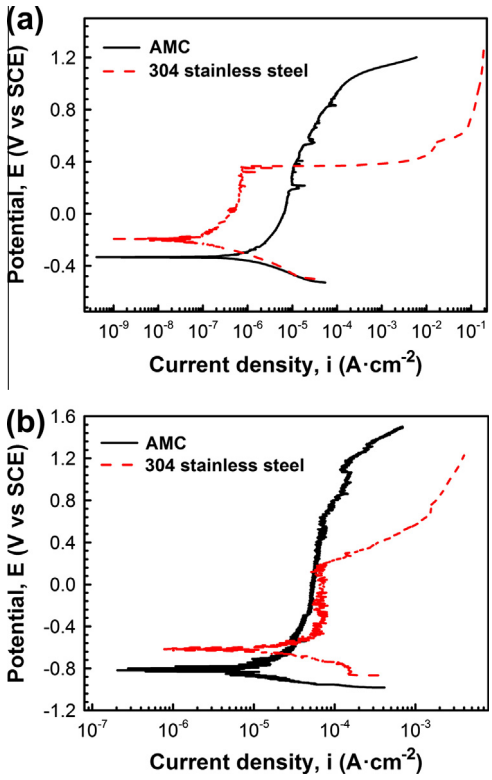

Fig. 6. Potentiodynamic polarisation curves of Fe-based AMC and 304 s.s. in a 3.5 wt.% NaCl solution under static immersion (a) and impingement condition (b) at 20 m/s.

Table 1
Summary of the electrochemical parameters obtained from potentiodynamic polarisation curves for 304 s.s. and Fe-based AMC in different conditions.

	E_{corr} (mV(SCE))	i_{corr} (A cm^{-2})	i_{pass} (A cm^{-2})	E_b (mV(SCE))
Static condition				
304 s.s.	−206	1.61×10^{-7}	6.11×10^{-7}	365
AMC	−332	1.25×10^{-6}	1.42×10^{-5}	1012
Under impingement				
304 s.s.	−623	1.27×10^{-5}	7.17×10^{-5}	203
AMC	−820	7.15×10^{-6}	6.09×10^{-5}	1052

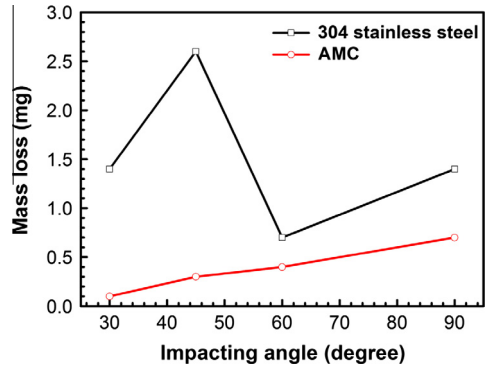

Fig. 7. Weight loss of Fe-based AMC and 304 s.s. as a function of impact angle in a 3.5 wt.% NaCl solution with 2 wt.% sand particles at 20 m/s for 8 h.

3.4. Current responses during erosion–corrosion

In order to evaluate the effect of impact velocity on AMC under erosion–corrosion, potentiostatic tests were carried out. Fig. 8 shows the current density responses of AMC (Fig. 8a) and 304 s.s. (Fig. 8b) at different impact velocities which were described in the experimental part. The potential applied in this test was 0 mV, which was in the passive range of both AMC and 304 s.s. under impingement according to the potentiodynamic tests above. For 304 s.s., before the velocity reaches to 12 m/s, the current density keeps at a relative low level. The current density decreases gradually with the increase of velocity up to 9 m/s. An abrupt rise appears when the velocity speeds up to 12 m/s and the following velocities. Large fluctuations of current densities are detected during high-speed impingement. For AMC, a similar trend is observed: a sudden rise in current density occurs at the velocity of 17 m/s. Although the current density fluctuates little before, it keeps almost at low values. According to some Refs. [37–39], current transients due to metastable pits are characterized by a rise, followed by a fast fall when the metastable pits repassivate. This indicates that fluctuations during the tests may result from the competitions between depassivation and repassivation. When depassivation dominates, the current density rises fast and will no long falls back, which means the loss of the protectiveness of passive film. The velocity which separates the two mechanisms is the critical fluid velocity under impingement. The responses of current densities present that the critical flow velocity of AMC is between 15 m/s and 17 m/s, higher than that of 304 s.s. which is between 9 m/s and 12 m/s under this experimental condition. The better repassivation ability of AMC may be one reason why it has a better erosion–corrosion resistance than 304 s.s. from the viewpoint of corrosion.

3.5. Synergistic effects of erosion and corrosion

Erosion–corrosion is not a simple addition of erosion and corrosion. The weight loss of erosion–corrosion is usually larger than the plus of erosion and corrosion. The excess part is called synergism

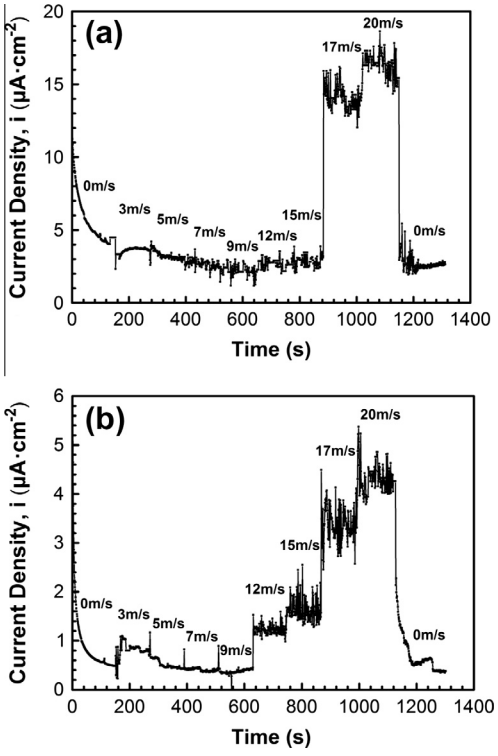

Fig. 8. Current density responses of Fe-based AMC (a) and 304 s.s. (b) measured with changes of impact velocities at a potential of 0 mV in a 3.5 wt.% NaCl solution containing 2 wt.% sand particles.

Table 2
Weight losses and percentages of pure corrosion (W_C), pure erosion (W_E), corrosion enhanced erosion (W_{COE}) and erosion enhanced corrosion (W_{EOC}) of 304 s.s. and Fe-based AMC under impingement at 20 m/s for 8 h.

Alloys	Weight loss (g m^{-2})					Percentage of damage (%)			
	W_T	W_C	W_E	W_{COE}	W_{EOC}	W_C/W_T	W_E/W_T	W_{COE}/W_T	W_{EOC}/W_T
304 s.s.	6.965	0.014	4.229	1.687	1.035	0.2	60.7	24.2	14.9
AMC	3.483	0.064	2.488	0.448	0.443	3	71.5	12.9	12.6

which may affect the erosion–corrosion a lot or even be decisive to the total damage. The synergistic weight loss can be calculated from the following equation:

$$W_T = W_C + W_E + W_{COE} + W_{EOC} \quad (1)$$

In the current work, the total weight loss (W_T) was measured under an impingement condition (3.5 wt.% NaCl solution + 2 wt.% sand particles). Pure erosion weight loss (W_E) was obtained from impingement result under a condition of 2 wt.% sand particles without NaCl containing. W_C was the pure corrosion weight loss which could be calculated from the i_{corr} in a static potentiodynamic test using the Faraday's law. According to Stack [40] and others [41–43], the synergism (W_S) between erosion and corrosion consists of the enhancement effect of erosion on corrosion (W_{EOC}) and enhancement effect of corrosion on erosion (W_{COE}). In present work, W_{EOC} was calculated from the i_{corr} which was detected by potentiodynamic test under impingement (W_C was deducted to work out W_{EOC}) and W_{COE} could be obtained from Eq. (1).

Table 2 shows the parameters described above under the 20 m/s impingement at normal angle for 8 h of both AMC and 304 s.s. It is clear that pure corrosion damage (W_C) of 304 s.s. is much lower than that of AMC. Once under a sand-containing impingement, 304 s.s. expresses weaker erosion–corrosion resistance than AMC by the values of pure erosion weight loss W_E and the synergism weight loss W_S ($W_{COE} + W_{EOC}$).

To analyse the components of erosion–corrosion, Table 2 also presents the weight loss percentages of each effect for AMC and 304 s.s. Generally speaking, pure erosion occupies the largest proportion for the total weight loss which indicates that mechanical effect of sand particles is the main factor for erosion–corrosion behaviour. Big difference occurs at the percentages of weight losses for corrosion–enhanced erosion (W_{COE}) and also the synergism (W_S). It is believed that W_{COE} is an enhancement of erosion damage by roughening the surface of material as a result of corrosion. Another reason for the severe erosion may be the partial or total removal of work hardening layer by the dissolution of corrosive

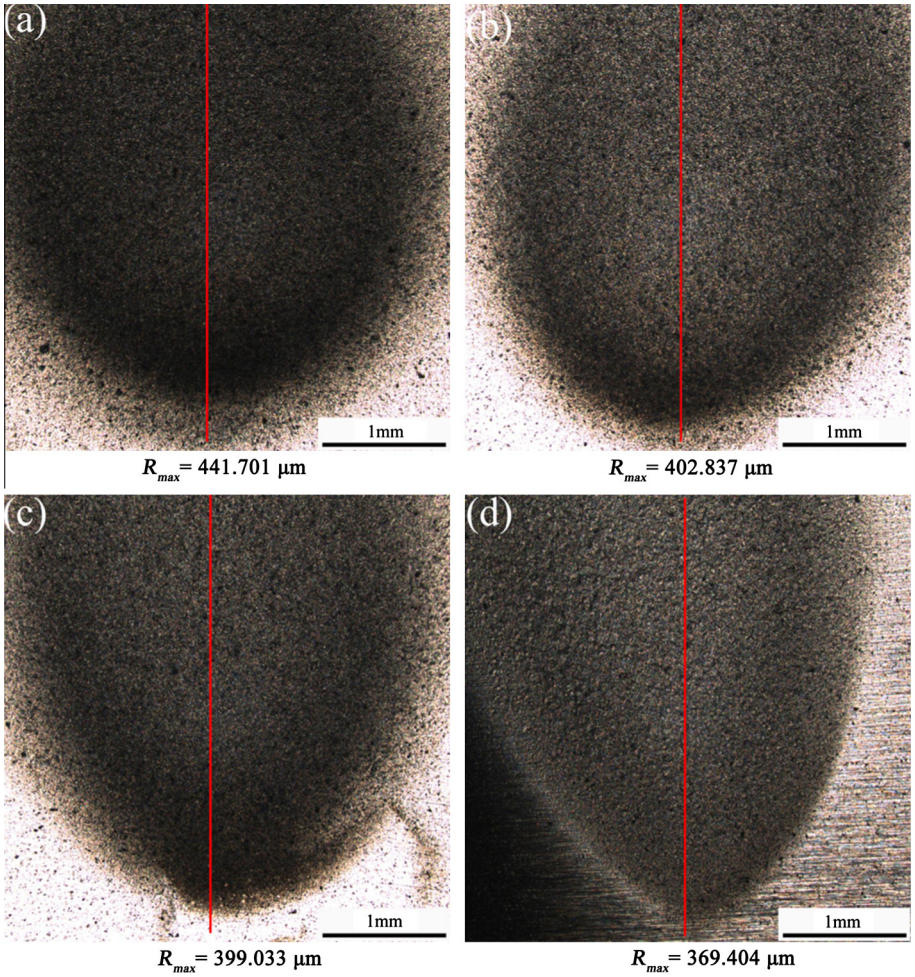

Fig. 9. Macro-morphologies of Fe-based AMC after impingement at 90° (a), 60° (b), 45° (c) and 30° (d) for 8 h. The pictures were taken using the Confocal Laser Scanning Microscope.

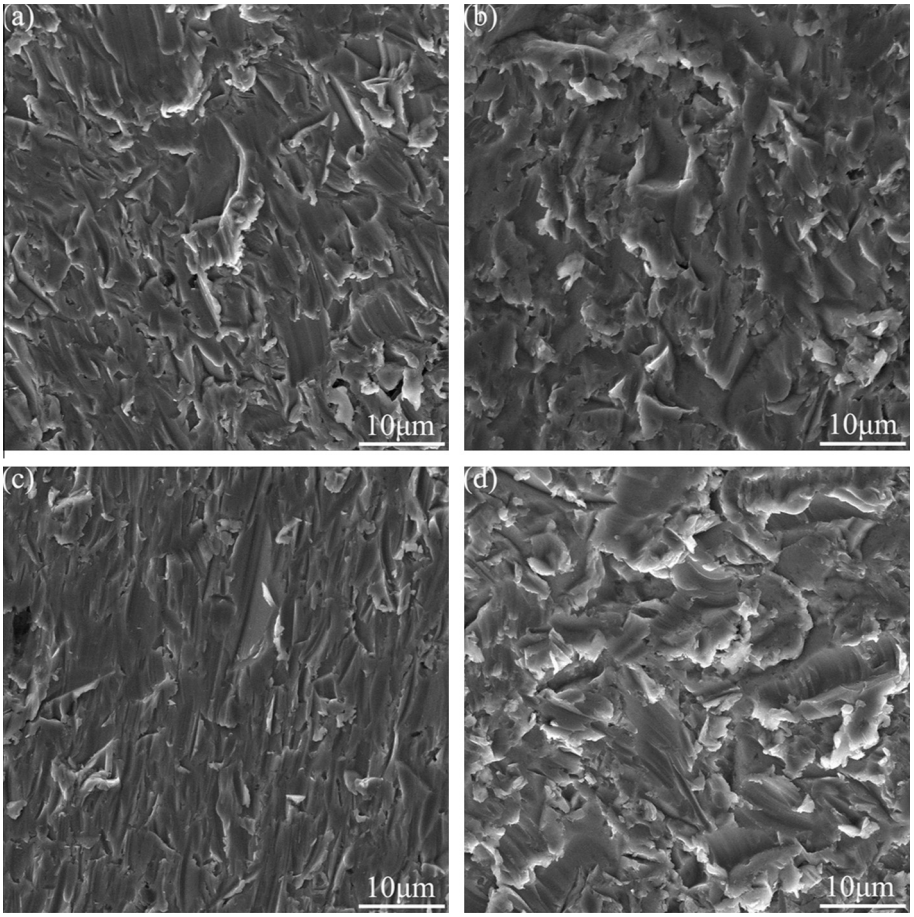

Fig. 10. Micro-morphologies of 304 s.s. after impingement at 30° (a), 45° (b), 60° (c) and 90° (d) for 8 h.

solution. In this work, compares to AMC, 304 s.s. has a crystal structure. The grain boundaries and phase boundaries may be corroded first and then causing the protrusions of grains and phases over the surfaces. The liquid–solid two phases flow impacts on the protrusive grains or phases and drops them out easily in the end. The large percentage of W_{COE} for 304 s.s. may also come from its low hardness. From the characterisations of coating, the hardness of AMC is about fourfold of 304 s.s. This may contribute to the relatively low values for all the erosion results of weight losses which contain W_E and W_{COE} of AMC. In contrast, the low hardness of 304 s.s. highlights its work hardening layer under impingement, therefore makes the effect of corrosion-enhanced erosion stand out as the work hardening layer is dissolved by corrosion.

Overall, the total weight loss of AMC is lower than that of 304 s.s., which suggests better erosion–corrosion resistance of AMC.

3.6. Erosion–corrosion morphology observations

Confocal Laser Scanning Microscope (CLSM) was applied to study the macro-morphology of Fe-based AMC after erosion–corrosion. Fig. 9 presents the results of Fe-based AMC after impingements at different angles by a sand-containing NaCl solution for 8 h. At 30°, a comet shape is developed and as the angle increases, the shape changes to a circular wear scar. While at all impact angles, erosion–corrosion degradations are both slighter at the inner round which is called the Laminar stagnation zone [44]. The parameter R_{max} which means the maximum of the distance between peak and valley of the surface along the measuring line (as highlighted) is also shown in Fig. 10. The values of R_{max} at different impingement angles present that the heaviest destruction appears under the impingement at 90° and in turn, followed by conditions at 60°, 45° and 30°. This agrees with the weight loss results shown in Section 3.3.

To assess the possible erosion–corrosion mechanisms for AMC and 304 s.s. under impingement at different impact angles, the worn surface of samples were studied by SEM. Fig. 10 shows the worn surface of 304 s.s. after 8 h of exposure to slurry flow (3.5 wt.% NaCl + 2 wt.% sand particles) with velocity of 20 m/s at different impact angles. It is obvious that the scratches at 30° (Fig. 10a) are shallower than others due to a smaller normal stress. When it comes to 45° as shown in Fig. 10b, relatively greater normal stress and shear stress leave the scars deeper. At the same time, lips formed during slurry erosion are effectively moved as shown in Fig. 10b compared to Fig. 10d, and the weight loss peak appears. Although the scratches occurred at 60° (Fig. 10c) are not fewer, the degrees of depth and width are smaller than others' and lips are scarcely seen in this condition. This information embodies in the minimum weight loss at the impact angle of 60°. The deep holes and lots of residual lips at 90° agree with the weight loss which is a peak value while not the biggest one among all results.

Fig. 11 shows the worn surfaces of Fe-based AMC after impingement at different angles. At the inclined angles like 30° and 45° which are shown in Fig. 11a and b, the scars are mostly short and shallow, and the quantity is fewer at 30°. At 60° as seen in Fig. 11c, cracks appear in directions which are not consistent with the scars. This phenomenon does not happen for 304 s.s. and it may be related to the unique stratified structure which contains pores, oxides and un-melted particles. The severest damage for Fe-based AMC under impingement is the scene as shown in Fig. 11d which is

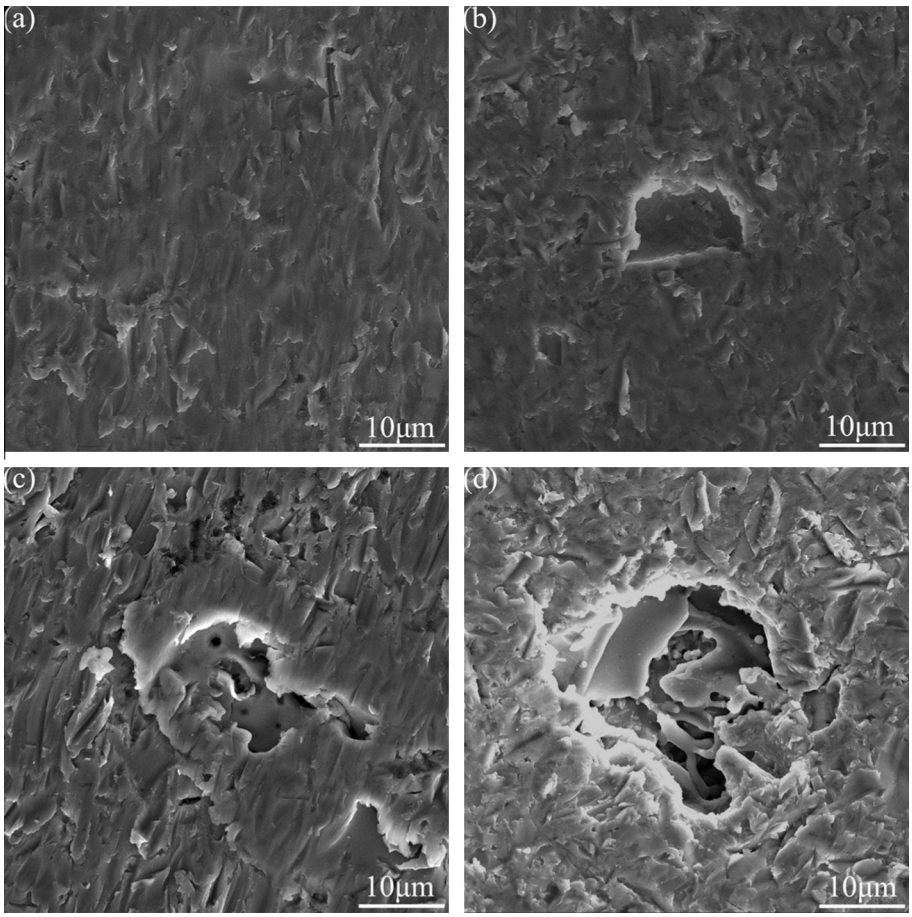

Fig. 11. Micro-morphologies of AMC after impingement at 30° (a), 45° (b), 60° (c) and 90° (d) for 8 h.

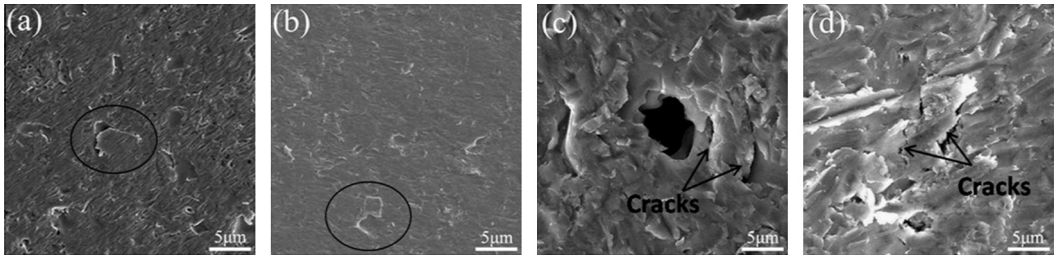

Fig. 12. Images showing some evidences of mechanisms of Fe-based AMC by particle impacts. (a and b) Impingement at oblique angle like 30° or 45°. (c and d) Impingement at large angle like 60° or 90°.

impacted at 90°. A strong slurry impacts on the weak areas like pores and enlarges them. While in other common areas, the high hardness makes erosion lightly, which is the reason why Fe-based AMC suffers a less weight loss compares to 304 s.s. under the same impingement conditions. The mechanisms for the impingements of Fe-based AMC and 304 s.s. at different angles will be further explored in discussion.

4. Discussion

4.1. Mechanisms of erosion–corrosion at different impact angles

In current work, two typical materials were studied under impingement at different impact angles, ductile material (304 s.s.) and brittle material (Fe-based AMC). The performances of them were obviously different due to their unique features.

For ductile material 304 s.s., several similar works have been done before and the trend of the weight loss had little deviation. It is believed that shear stress and normal stress are key effects on the surface of materials under impingement. The synergism of them comes to be the largest at 45°. Once the flakes formed from the extrusion effect of normal stress, they are easily cut off by the strong shear stress. At the impact angle of 30–45°, as the angle increases, the normal stress increases and so does the weight loss. The changes indicate that the effect of normal stress dominates the erosion–corrosion process at these impact angles. The leading role turns to be the shear stress which decreases by the increase of angles between 45° and 90°. Because of the reduction of cutting effect, more materials are residual on the surface and results in a decrease of weight loss as the angle increases from 45° to 90°. Little difference occurs when the stainless steel is under impingement at the impact angle between 60° and 90°. Burstein and Sasaki [20]

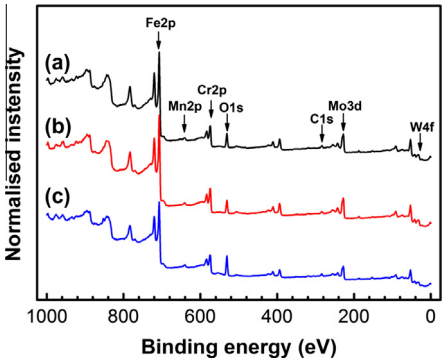

Fig. 13. Wide scan XPS spectra for Fe-based AMC polarised at 0 V for an hour in a 3.5 wt.% NaCl solution (a), under impingement at 10 m/s (b) and 20 m/s (c).

found a minimum of weight loss for 304 s.s. under erosion–corrosion at 90° and they considered that most of the passive film remained on the scar and merely to be broken. But Tang et al. [21] studied the erosion–corrosion of X-65 steel and discovered that at 90°, the normal stress established was the highest and was sufficient to result in a high erosion–corrosion rate which was consistent with the current work. The aspects they analysed were of both feasibility, but in this work, some possibilities may contribute to the lowest weight loss at 60° and the increase of weight loss as the impact angle increases during 60–90° besides the reason stated by Tang et al. [21]. According to Clack's work [45], although the angle of the flowing to the material surface was set at 90°, the exact angles of sand particles impact on surface did not all keep the same with the liquid flow. For several sizes of particles, all impact angles between 90° and 0° would be present during this condition. This may explain why long scratches and cutting action appear at 90° in Fig. 10d. The unexpected existence of cutting effect at 90° may remove the broken passive film which remains adherent and lead to a larger weight loss. This may be the reason why the lowest weight loss appears at 60° instead of 90°.

For AMC, the brittleness is inherited from the amorphous structure and due to the occurrence of nanocrystallines, the hardness is enhanced much. The maximum weight loss appears at normal angle impact. In other words, the shear stress resistance of Fe-based AMC is excellent and the normal stress plays key role during the impingement. Two mechanisms for the erosion–corrosion behaviour of Fe-based AMC are built up according to its performances at different impact angles. One is the impingement at oblique angle like 30° or 45°, and another is at 60° or 90° which is normal. In the former situation, sand particles impact the surface of coating from oblique angles and leave shallow scars due to the high hardness of the coating. It is notable that some shallow holes are detected out in these cases as clearly shown in Figs. 11b and 12a and b. They are always of no features, with no scars in them and it looks like that they are newly developed. The EDS result which does not present here shows that the main compositions of these no features places are oxides which are distinct from other areas. Considered with the oxides mentioned in Section 3.1, it is reasonable to infer that the oxides are the division of different layers of the coating. Therefore it comes to a conclusion that under the impingement at oblique angles, the passive films are destroyed and removed from the surface first and then the weak boundaries of oxide layer expose. Repeated impacts and the penetration of corrosive Cl^- containing solution lead to the separation of the oxide layer and the lamellar coatings above it. Due to the relatively low binding strength of different layers, lamellar coatings flake off in the end. Some moments are luckily caught by SEM as shown in Fig. 12a and b, corresponding to the erosion–corrosion mechanism. When the impact angle increases to 60° or larger, the dominant factor has changed. On one side, with the normal stress becomes stronger, particles strike harder onto the surface and make it rougher. On the other side, the energy absorbed from the kinetic energy of impact particles promotes brittle cracks derive from the defects of the coating like pores or pits after corrosion. These cracks propagate in different way both in the surface and longitudinal section and finally meet each other in the coating. Tangles of cracks lead to brittle failures in the end. Serious damages with large area and deep crater are usually caused as seen in Figs. 11c and 12c and d.

4.2. Critical flow velocities and passive films under impingement

The critical flow velocities of Fe-based AMC and 304 s.s. were detected out through electrochemical measurements under impingement at the normal angle in a 3.5 wt.% NaCl solution containing 2 wt.% sand. Taking the passivation into consideration, the applied potential impels the passivation on surface of material. Once under a sand containing impingement, at one time, the cathodic reaction is accelerated because of increasing the weight transfer rate of dissolved oxygen by reducing the thickness of the

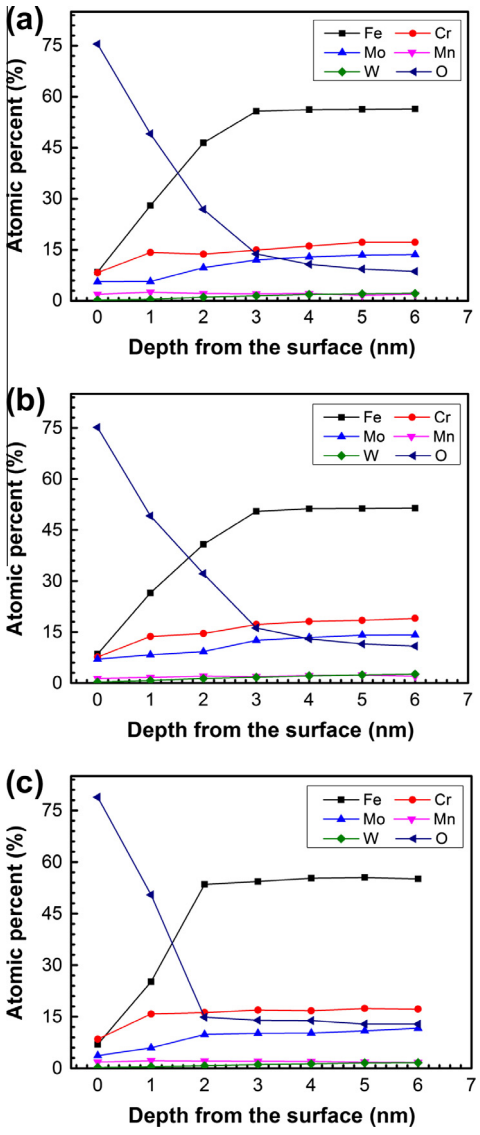

Fig. 14. Depth profiles of elements for the passive film grown on Fe-based AMC polarised at 0 V for an hour in a 3.5 wt.% NaCl solution (a), under impingement at 10 m/s (b) and 20 m/s (c).

diffusion layer [17], at another time, the passive film formed on the surface may suffer mechanical damage by sand particles. These effects result in a competition between damage and regeneration of the passive film, which are called depassivation and repassivation. In current work, when the impact velocity is smaller than 15 m/s (for AMC), the current density as a result of depassivation and repassivation, keeps at a low level. After changing the velocity to a value larger than the critical one, the current density increases hard and something must have happened to the passive film. This change may also contribute to an enlargement for weight loss and other parameters [24,25,46].

In order to study the possible relationship between the velocity and the passive film under erosion–corrosion, XPS was used to analyse the formation of passive film on surface of Fe-based AMC. The samples were disposed in three ways: one was just immersed in 3.5 wt.% NaCl and polarised at 0 V for an hour; the other two were polarised under the impingement at the same potential for an hour, but the impact velocities were of little difference, one was 10 m/s (sample b) which was smaller than the critical velocity and the other one was 20 m/s (sample c), higher than the critical value. Fig. 13 shows the normalised XPS survey spectra of the three samples after Ar ions sputtering for 20 s. Some main peaks are marked in the spectra which indicate the presence of Fe, Cr, Mo, Mn, W, O and C. It is obvious that the wide scans of these three samples are almost the same, both the positions of the peaks and the strength of each peak. The result demonstrates that the passive films formed on these conditions are almost the same in the aspect of composition. Difference occurs in the depth profiles of elements as shown in Fig. 14. The observed elements: Fe, Cr, Mo, Mn and W, which are the main elements of passive films as discussed in our early work [14], present similar changes in these three samples. They all increase at first and are nearly constant in the end from the surface to the matrix. But the content of O decreases first and remains at a low level in the inner part of the samples. If the depth before the metallic elements are constant is defined as the thickness of passive film, the thickness of passive film on sample (a) and sample (b) are near 3 nm, larger than that of sample (c) which is about 2 nm. Together with the critical flow velocity, the results indicate that the passive film formed on the surface of Fe-based AMC can repair itself timely under impingement at a velocity smaller than the critical value. The newly developed film is almost the same with the static one and can protect effectively against erosion–corrosion. During a high speed impact, the repassivation is weaker and the newly formed passive film is thinner. The film can be destroyed easily and severe damages occur into the material before the film is repaired completely. The critical flow velocity may be the separation of the two cases above. From this viewpoint, the materials with larger critical value may present better erosion–corrosion resistance for the stronger ability of repassivation. This may be one reason why Fe-based AMC exhibits better erosion–corrosion resistance than 304 s.s.

5. Conclusions

(1) Fe-based AMC exhibits good resistance to erosion–corrosion. The weight loss of it is much less than that of 304 s.s. under impingement in a sand-containing NaCl solution. The higher resistance to E–C of AMC may be due to the higher hardness as well as better repassivation ability under impingement.

(2) Erosion–corrosion behaviour depends on the impact angle. The weight loss of the AMC increases with the impact angle up to the peak value of 90°. Different damage mechanisms exist due to the structure and properties of the coating at different impact angles. The weight loss peak of 304 s.s. appears at 45° due to the strong synergism of shear stress and normal stress acting on the surface.

(3) The main damages of AMC and 304 s.s. under impingement are caused by the effect of pure erosion. The percentage of the synergism of 304 s.s. is larger than that of AMC. The passive current density of AMC under impingement increases about 10 times in contrast with 100 times for 304 s.s.

(4) The critical flow velocity of Fe-based AMC is about 15 m/s under impingement in a 2 wt.% sand containing 3.5 wt.% NaCl solution, higher than that of 304 s.s. which is about 9 m/s. The passive film formed under impingement at a velocity below the critical value is thicker, which may be related to the domination of repassivation during erosion–corrosion behaviour.

Acknowledgements

This work was supported by the National Natural Science Foundation of China (No. 51131008). The authors would like to acknowledge valuable suggestions from Dr. D. Fan.

References

[1] C.J. Wong, J.C.M. Li, Wear behaviour of an amorphous alloy, Wear 98 (1984) 45–61.
[2] B. Prakash, Abrasive wear behaviour of Fe, Co and Ni based metallic glasses, Wear 258 (2005) 217–224.
[3] S.J. Pang, T. Zhang, K. Asami, A. Inoue, Synthesis of Fe–Cr–Mo–C–B–P bulk metallic glasses with high corrosion resistance, Acta Materialia 50 (2002) 489–497.
[4] Z.F. Zhang, J. Eckert, L. Schultz, Difference in compressive and tensile fracture mechanisms of Zr59CU20Al10Ni8Ti3 bulk metallic glass, Acta Materialia 51 (2003) 1167–1179.
[5] J. Farmer, F. Wong, J. Haslam, J. Estill, D. Branagan, N. Yang, C. Blue, Development, processing and testing of high-performance corrosion-resistant HVOF coatings, in: Global 2003 Topical Meeting at the American Nuclear Society Conference, 2003.
[6] M. Cherigui, N.E. Fenineche, C. Coddet, Structural study of iron-based microstructured and nanostructured powders sprayed by HVOF thermal spraying, Surface and Coatings Technology 192 (2005) 19–26.
[7] Z. Zhou, L. Wang, F.C. Wang, H.F. Zhang, Y.B. Liu, S.H. Xu, Formation and corrosion behaviour of Fe-based amorphous metallic coatings by HVOF thermal spraying, Surface and Coatings Technology 204 (2009) 563–570.
[8] Y. Yang, C. Zhang, Y. Peng, Y. Yu, L. Liu, Effects of crystallization on the corrosion resistance of Fe-based amorphous coatings, Corrosion Science 59 (2012) 10–19.
[9] G. Bolelli, L. Lusvarghi, R. Giovanardi, A comparison between the corrosion resistances of some HVOF-sprayed metal alloy coatings, Surface and Coatings Technology 202 (2008) 4793–4809.
[10] Y. Wang, S.L. Jiang, Y.G. Zheng, W. Ke, W.H. Sun, J.Q. Wang, Electrochemical behaviour of Fe-based metallic glasses in acidic and neutral solutions, Corrosion Science 63 (2012) 159–173.
[11] Z.M. Wang, Y.T. Ma, J. Zhang, W.L. Hou, X.C. Chang, J.Q. Wang, Influence of yttrium as a minority alloying element on the corrosion behaviour in Fe-based bulk metallic glasses, Electrochimica Acta 54 (2008) 261–269.
[12] W. Yuping, L. Pinghua, C. Chenglin, W. Zehua, C. Ming, H. Junhua, Cavitation erosion characteristics of a Fe–Cr–Si–B–Mn coating fabricated by high velocity oxy-fuel (HVOF) thermal spray, Materials Letters 61 (2007) 1867–1872.
[13] X.Q. Liu, Y.G. Zheng, X.C. Chang, W.L. Hou, J.Q. Wang, Z. Tang, A. Burgess, Microstructure and properties of Fe-based amorphous metallic coating produced by high velocity axial plasma spraying, Journal of Alloys and Compounds 484 (2009) 300–307.
[14] Y. Wang, Y.G. Zheng, W. Ke, W.H. Sun, W.L. Hou, X.C. Chang, J.Q. Wang, Slurry erosion–corrosion behaviour of high-velocity oxy-fuel (HVOF) sprayed Fe-based amorphous metallic coatings for marine pump in sand-containing NaCl solutions, Corrosion Science 53 (2011) 3177–3185.
[15] F. Mohammadi, J. Luo, B. Lu, A. Afacan, Single particle impingement current transients for prediction of erosion–enhanced corrosion on 304 stainless steel, Corrosion Science 52 (2010) 2331–2340.
[16] M.M. Stack, T.M.A. El-Badia, Some comments on mapping the combined effects of slurry concentration, impact velocity and electrochemical potential on the erosion–corrosion of WC/Co–Cr coatings, Wear 264 (2008) 826–837.
[17] K. Sasaki, G.T. Burstein, Erosion–corrosion of stainless steel under impingement by a fluid jet, Corrosion Science 49 (2007) 92–102.
[18] A. Neville, T. Hodgkiess, An assessment of the corrosion behaviour of high-grade alloys in seawater at elevated temperature and under a high velocity impinging flow, Corrosion Science 38 (1996) 927–956.
[19] R.J.K. Wood, A.J. Speyer, Erosion–corrosion of candidate HVOF aluminium-based marine coatings, Wear 256 (2004) 545–556.

[20] G.T. Burstein, K. Sasaki, Effect of impact angle on the slurry erosion–corrosion of 304L stainless steel, Wear 240 (2000) 80–94.
[21] X. Tang, L.Y. Xu, Y.F. Cheng, Electrochemical corrosion behaviour of X-65 steel in the simulated oil–sand slurry. II: Synergism of erosion and corrosion, Corrosion Science 50 (2008) 1469–1474.
[22] H.X. Hu, S.L. Jiang, Y.S. Tao, T.Y. Xiong, Y.G. Zheng, Cavitation erosion and jet impingement erosion mechanism of cold sprayed Ni–Al_2O_3 coating, Nuclear Engineering and Design 241 (2011) 4929–4937.
[23] X. Hu, A. Neville, The electrochemical response of stainless steels in liquid–solid impingement, Wear 258 (2005) 641–648.
[24] Y.G. Zheng, F. Yang, Z.M. Yao, W. Ke, On the critical flow velocity of Cu–Ni alloy BFe30-1-1 in flowing artificial seawater, Zeitschrift Für Metallkunde 91 (4) (2000) 323–328.
[25] X. Jiang, Y.G. Zheng, W. Ke, Effect of flow velocity and entrained sand on inhibition performances of two inhibitors for CO_2 corrosion of N80 steel in 3% NaCl solution, Corrosion Science 47 (2005) 2636–2658.
[26] Y. Wang, S.L. Jiang, Y.G. Zheng, W. Ke, W.H. Sun, J.Q. Wang, Effect of porosity sealing treatments on the corrosion resistance of high-velocity oxy-fuel (HVOF)-sprayed Fe-based amorphous metallic coatings, Surface and Coatings Technology 206 (2011) 1307–1318.
[27] R.Q. Guo, C. Zhang, Q. Chen, Y. Yang, N. Li, L. Liu, Study of structure and corrosion resistance of Fe-based amorphous coatings prepared by HVAF and HVOF, Corrosion Science 53 (2011) 2351–2356.
[28] A. Inoue, High-strength bulk amorphous-alloys with low critical cooling rates, Materials Transactions Jim 36 (1995) 866–875.
[29] Y.P. Wu, P.H. Lin, G.Z. Xie, J.H. Hu, M. Cao, Formation of amorphous and nanocrystalline phases in high velocity oxy-fuel thermally sprayed a Fe–Cr–Si–B–Mn alloy, Materials Science and Engineering: A 430 (2006) 34–39.
[30] G.C. Saha, T.I. Khan, G.A. Zhang, Erosion–corrosion resistance of microcrystalline and near-nanocrystalline WC-17Co high velocity oxy-fuel thermal spray coatings, Corrosion Science 53 (2011) 2106–2114.
[31] M.M. Verdian, K. Raeissi, M. Salehi, Corrosion performance of HVOF and APS thermally sprayed NiTi intermetallic coatings in 3.5% NaCl solution, Corrosion Science 52 (2010) 1052–1059.
[32] C. Zhang, R.Q. Guo, Y. Yang, Y. Wu, L. Liu, Influence of the size of spraying powders on the microstructure and corrosion resistance of Fe-based amorphous coating, Electrochimica Acta 56 (2011) 6380–6388.
[33] Y. Li, G.T. Burstein, I.M. Hutchings, The influence of corrosion on the erosion of aluminum by aqueous silica slurries, Wear 186 (1995) 515–522.
[34] M.M. Stack, Y. Purandare, P. Hovsepian, Impact angle effects on the erosion–corrosion of superlattice CrN/NbN PVD coatings, Surface and Coatings Technology 188 (2004) 556–565.
[35] Y. Purandare, M.M. Stack, P. Hovsepian, A study of the erosion–corrosion of PVD CrN/NbN superlattice coatings in aqueous slurries, Wear 259 (2005) 256–262.
[36] R.G. Wellman, C. Allen, The effects of angle of impact and material properties on the erosion fates of ceramics, Wear 186 (1995) 117–122.
[37] G.T. Burstein, K. Sasaki, The birth of corrosion pits as stimulated by slurry erosion, Corrosion Science 42 (2000) 841–860.
[38] X.M. Hu, A. Neville, An examination of the electrochemical characteristics of two stainless steels (UNS S32654 and UNS S31603) under liquid–solid impingement, Wear 256 (2004) 537–544.
[39] J. Xu, C.Z. Zhuo, D.Z. Han, J. Tao, L.L. Liu, S.Y. Jiang, Erosion–corrosion behaviour of nano-particle-reinforced Ni matrix composite alloying layer by duplex surface treatment in aqueous slurry environment, Corrosion Science 51 (2009) 1055–1068.
[40] M.M. Stack, G.H. Abdulrahman, Mapping erosion–corrosion of carbon steel in oil exploration conditions: some new approaches to characterizing mechanisms and synergies, Tribology International 43 (2010) 1268–1277.
[41] B.T. Lu, J.F. Lu, J.L. Luo, Erosion–corrosion of carbon steel in simulated tailing slurries, Corrosion Science 53 (2011) 1000–1008.
[42] V.A.D. Souza, A. Neville, Corrosion and synergy in a WCCoCr HVOF thermal spray coating—understanding their role in erosion–corrosion degradation, Wear 259 (2005) 171–180.
[43] S.S. Rajahram, T.J. Harvey, R.J.K. Wood, Erosion–corrosion resistance of engineering materials in various test conditions, Wear 267 (2009) 244–254.
[44] E.A.M. Hussain, M.J. Robinson, Erosion–corrosion of 2205 duplex stainless steel in flowing seawater containing sand particles, Corrosion Science 49 (2007) 1737–1754.
[45] H.M. Clark, The influence of the flow field in slurry erosion, Wear 152 (1992) 223–240.
[46] X. Ji, J. Zhao, X. Zhang, M. Zhou, Erosion–corrosion behaviour of Zr-based bulk metallic glass in saline-sand slurry, Tribology International 60 (2013) 19–24.